

Supporting information

Highly Exposed Discrete Co Atoms Anchored in Ultrathin Porous N, P-Codoped Carbon Nanosheet for Efficient Oxygen Electrocatalysis and Rechargeable Aqueous/Solid-State Zn-Air Batteries

*Xinghuan Liu^[+]^a, Yanwen Zhang^[+]^a, Zeyu Zhao^a, Haoran Gao^a, Junjie Kang^a, Rongjie Wang^a, Guixian Ge^b, Xin Jia^{*a}*

^aSchool of Chemistry and Chemical Engineering/Key Laboratory for Green Processing of Chemical Engineering of Xinjiang Bingtuan, Key Laboratory of Materials-Oriented Chemical Engineering of Xinjiang Uygur Autonomous Region, Engineering Research Center of Materials-Oriented Chemical Engineering of Xinjiang Bingtuan, Shihezi University, Shihezi 832003, China. E-mail: jiaxin@shzu.edu.cn.

^bKey Laboratory of Ecophysics and Department of Physics, College of Science, Shihezi University, Shihezi, 832003, P. R. China. E-mail: geguixian@126.com.

[+] These authors contributed equally to this work.

1. Characterization

Scanning electron microscopy images were acquired on a SEM (Hitachi SU8010 Japan). Transmission electron microscopy (Hitachi HT7700 Japan) was used to observe the morphologies of the catalysts. The dispersed state of Co atoms was observed on high-resolution transmission electron microscopy (HRTEM, JEM ARM 200F, JEOL Inc., Japan). The morphologies of the catalysts were characterized by aberration-corrected scanning transmission electron microscopy (AC-STEM) equipped with an energy dispersive X-ray spectrometer (EDS) on FEI Titan Cubed Themis G2 300. XRD patterns at wide angles (10–90°) were collected using a Bruker D8 advanced X-ray diffractometer with Cu K α irradiation at 40 kV and 40 mA. X-ray photoelectron spectroscopy (XPS) was performed using an Axis Ultra spectrometer with a mono-chromatized Al K α X-ray as the excitation source (225 W). Brunauer–Emmett–Teller (BET) specific surface areas were measured by nitrogen adsorption–desorption analyses using a micromeritics ASAP 2020. Raman spectra were measured on a LabRAM HR Evolution Raman microscope with 514.5 nm laser excitation in the range of 500–2000 cm⁻¹. The X-ray absorption data at the Fe K-edge of the samples were recorded at room temperature in transmission mode using ion chambers (referenced samples) and fluorescence excitation mode using a Lytle detector (controlled samples) at beamline BL14W1 of the Shanghai Synchrotron Radiation Facility (SSRF). The station was operated with a Si (111) double crystal monochromator. During the measurement, the synchrotron was operated at 3.5 GeV and the current was between 150-210 mA. The data for each sample were calibrated with standard Fe metal foil. Data processing was performed using the program ATHENA. Extended X-ray absorption fine structure (EXAFS) spectra were fitted using the FEFF 6.0 code.

2. Electrochemical measurements

All of the electrochemical measurements were performed with a CHI 760E electrochemical analyzer (Cheng Hua Instruments, Inc., Shanghai, China) at room temperature. Electrochemical measurements were performed in a conventional three electrode cell by using

Ag/AgCl (saturated KCl) as the reference electrode, a platinum wire as the counter electrode and catalysts coated glassy carbon (GC, 3.0 mm diameter) electrodes as the working electrodes. To prepared the working electrodes, 3.0 mg of catalysts were dispersed ultrasonically for 30 min in a mixture solution of ethanol (600 μ l) and Nafion (5 wt%, 30 μ l). 5 μ l well-dispersed mixture was dropped onto glassy carbon electrode with a catalyst loading of 0.337 mg cm^{-2} and then fully dried at room temperature. For the OER, the polarization curves were also measured in 0.1 M KOH solution recorded from 1.0 to 2.0 V at a scan rate of 5 mV s^{-1} . The high-purity O_2 is bubbled through the electrolyte during the testing to fix the reversible oxygen potential (or ensure the $\text{O}_2/\text{H}_2\text{O}$ equilibrium at 1.23 V vs. RHE). To avoid the peeling of catalyst caused by evolved O_2 adhesion, a rotation speed of 1600 rpm was offered during the OER. For ORR, Cyclic voltammetry (CV) and linear sweep voltammetry (LSV) were conducted with a sweep rates of 50 mV/s and 5 mV/s, respectively. All electrochemical tests were measured in N_2 or O_2 -saturated 0.1 M KOH or 0.1 M HClO_4 aqueous solution at room temperature.

The electron transfer number (n) and kinetic current density (J_k) were investigated based on the Koutecky–Levich (K–L) equation:

$$1/J = 1/J_k + 1/J_L = 1/B\omega^{1/2} + 1/J_k \quad (1)$$

$$B=0.2nFC_0(D_0)^{2/3}\nu^{-1/6} \quad (2)$$

where J is the measured current density, J_k and J_L are the kinetic and diffusion-limiting current densities, ω is the rotating speed of the disk, F is the Faraday constant (96,485 C mol^{-1}); C_0 is the bulk concentration of O_2 (1.2×10^{-3} M in 0.1 mol L^{-1} KOH, and 1.26×10^{-3} M in 0.1 mol L^{-1} HClO_4), D_0 is the diffusion coefficient of O_2 (1.9×10^{-5} $\text{cm}^2 \text{s}^{-1}$ in 0.1 mol L^{-1} KOH and 1.93×10^{-5} $\text{cm}^2 \text{s}^{-1}$ in 0.1 mol L^{-1} HClO_4); and ν is the kinematic viscosity of the electrolyte ($0.01 \text{ cm}^2 \text{s}^{-1}$ in 0.1 mol L^{-1} KOH and $1.009 \times 10^{-2} \text{ cm}^2 \text{s}^{-1}$ in 0.1 mol L^{-1} HClO_4).

The electron transfer number and hydrogen peroxide yield ($\%\text{H}_2\text{O}_2$) during the ORR can be determined by the RRDE technique:

$$\text{H}_2\text{O}_2 (\%) = \frac{200 \times \frac{I_{Ring}}{N}}{I_{Disk} + \frac{I_{Ring}}{N}} \quad (3)$$

$$n = \frac{4 \times I_{Disk}}{I_{Disk} + \frac{I_{Ring}}{N}} \quad (4)$$

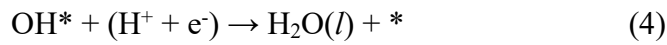
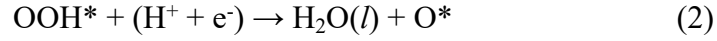
where I_d is the disk current, I_r is the ring current, and $N = 0.37$ is the current collection efficiency of the Pt ring.

All potentials were referenced to the reversible hydrogen electrode (RHE) through RHE calibration: $E(\text{RHE}) = E(\text{Ag}/\text{AgCl}) + 0.198 + 0.059 \times \text{pH}$.

3. Computational details

All spin-polarized density functional theory (DFT) method was employed to obtain the geometric optimizations using the Vienna ab initio simulation package (VASP).^[1, 2] The electron exchange-correlation is represented by the functional of Perdew-Burke-Ernzerhof (PBE) of generalized gradient approximation (GGA).^[3] The projector augmented wave (PAW) pseudo-potentials were used to describe ionic cores.^[2] The Co single atom on nitrogen-doped carbon ($\text{Co}_{\text{SA}}/\text{NC}$) and Co atom supported on nitrogen/ phosphorus co-doped carbon ($\text{Co}_{\text{SA}}/\text{NPC}$) monolayer were modeled by using $6 \times 6 \times 1$ supercell and Brillouin zones was sampled with $2 \times 2 \times 1$ grid centered at the gamma (Γ) point in reciprocal space for geometry optimization. A vacuum region more than 20 Å along the z-axis was set to prevent the interaction between two adjacent periodic images. A cut-off energy of 450 eV was adopted for the plane-wave basis. The Van der Waals (vdW) interactions have been considered with Grimme's semiempirical DFT-D3 scheme.^[4] The convergence tolerances for energy and force were set to 10^{-5} eV and 0.02 eV/Å, respectively. The Gibbs free energy change (ΔG) for each of the oxygen reduction reaction (ORR) steps was estimated applying the computational

hydrogen electrode (CHE) model of Nørskov et al.^[5] The CHE model uses one half of chemical potential of gaseous hydrogen ($\mu(\text{H}_2)$) as the chemical potential of the proton-electron pair ($\mu(\text{H}^+ / e^-)$). The reaction scheme of the ORR in acidic media at zero electrode potential can be written as:



In alkaline media, the elementary steps are:



According to CHE model, the ΔG values for each ORR step were defined as

$$\Delta G = \Delta E_{\text{DFT}} + \Delta E_{\text{ZPE}} - T\Delta S + \Delta G_{\text{U}} + \Delta G_{\text{pH}} \quad (9)$$

In this equation, ΔE_{DFT} is the reaction energy of reactant and product molecules adsorbed on catalyst surface, obtained from DFT calculations. ΔE_{ZPE} and ΔS are the change in the zero-point energy (ZPE) and entropy at the room temperature ($T = 298.15 \text{ K}$), which are obtained after frequency calculations. ΔG_{U} is the free energy contribution related to the applied electrode potential (U). ΔG_{pH} is the Gibbs free energy change caused by pH value, which was calculated by

$$\Delta G_{\text{pH}} = \ln 10 \times k_{\text{B}}T \times \text{pH} \quad (10)$$

where k_B is the Boltzmann constant. Hence, the equilibrium potential (U_0) for four electron transfer ORR at pH = 0 and pH = 14 were determined to be 1.229 and 0.401 V versus NHE, respectively.

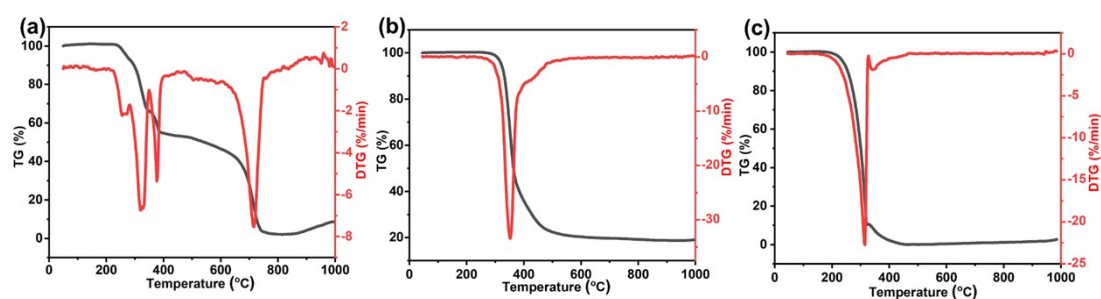


Figure S1 TG and DTG spectra of (a) dicyandiamide (DCDA), (b) dopamine (DA) and (c) triphenyl phosphine (TPP).

TG and DTG results reveal that DA still have about 20% carbonization product (Figure S1b), indicating that DA is a potential precursor. TG and DTG spectrum of TPP show sharp decline between 200 and 400 °C (Figure S1c), it decomposed completely after 1000 °C.

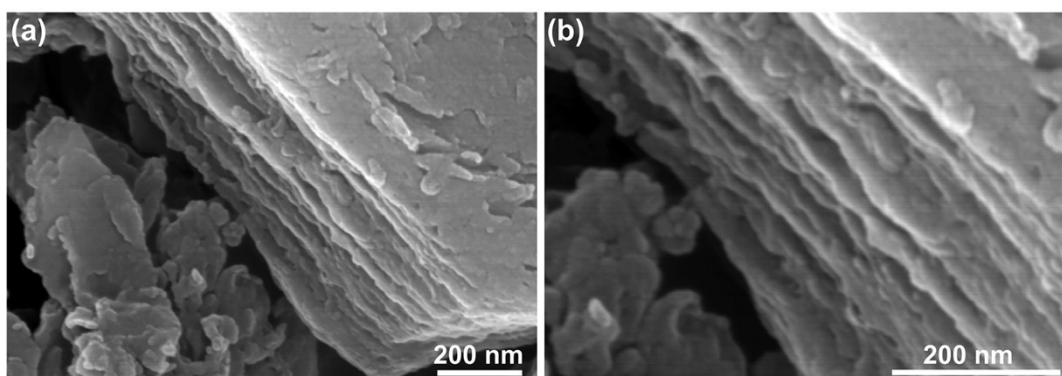


Figure S2 SEM images of Co, N, P doped carbon/g-C₃N₄ composites obtained at 600 °C.

The Co, N, P doped carbon/g-C₃N₄ composites were obtained by pyrolyzation the mixture of DCDA, DA/Co²⁺ and TPP at 600 °C. The typical layered structure of g-C₃N₄ can also be observed in the composite, indicating the well development of polymeric plane of carbon nitride even with the presence of DA/Co²⁺ and TPP or as-formed aromatic carbon intermediates.

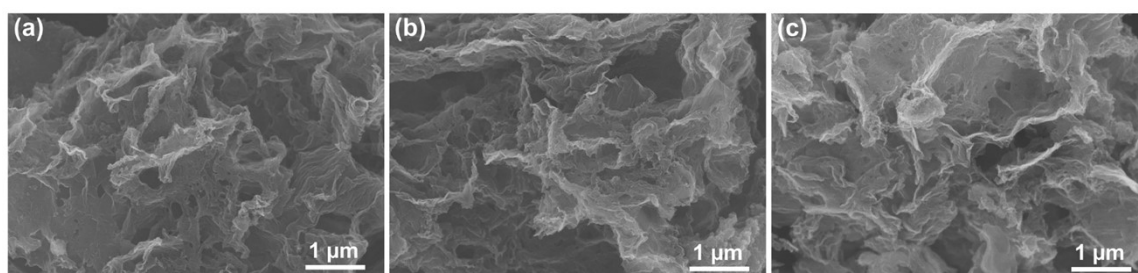


Figure S3 SEM images of Co/NC, NPC and NC, respectively.

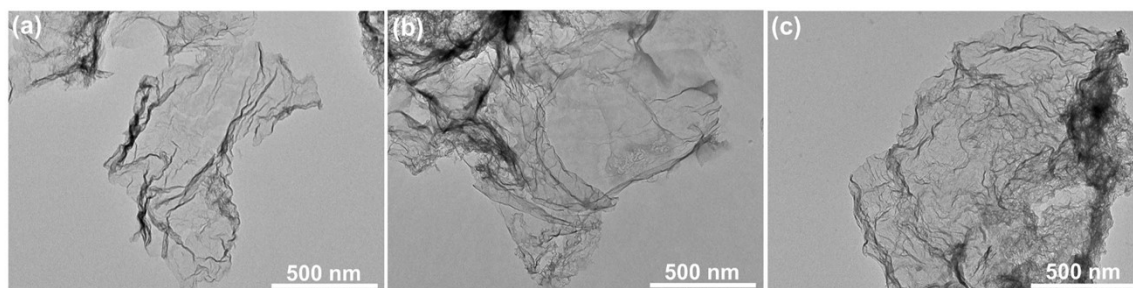


Figure S4 TEM images of Co/NC, NPC and NC, respectively.

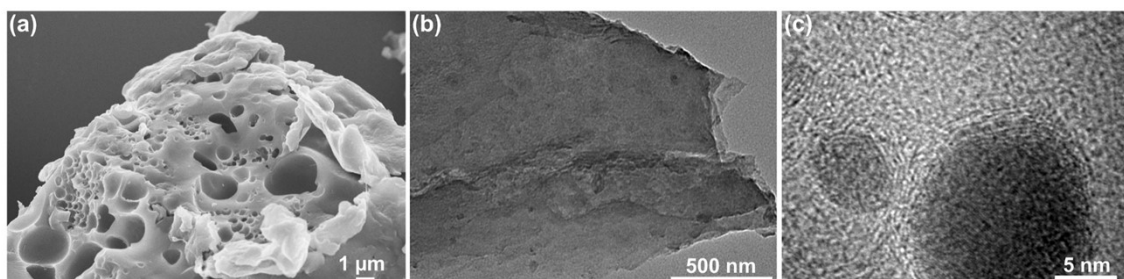


Figure S5 (a) SEM, (b) TEM and (c) HRTEM images of Co/NPC-NNS.

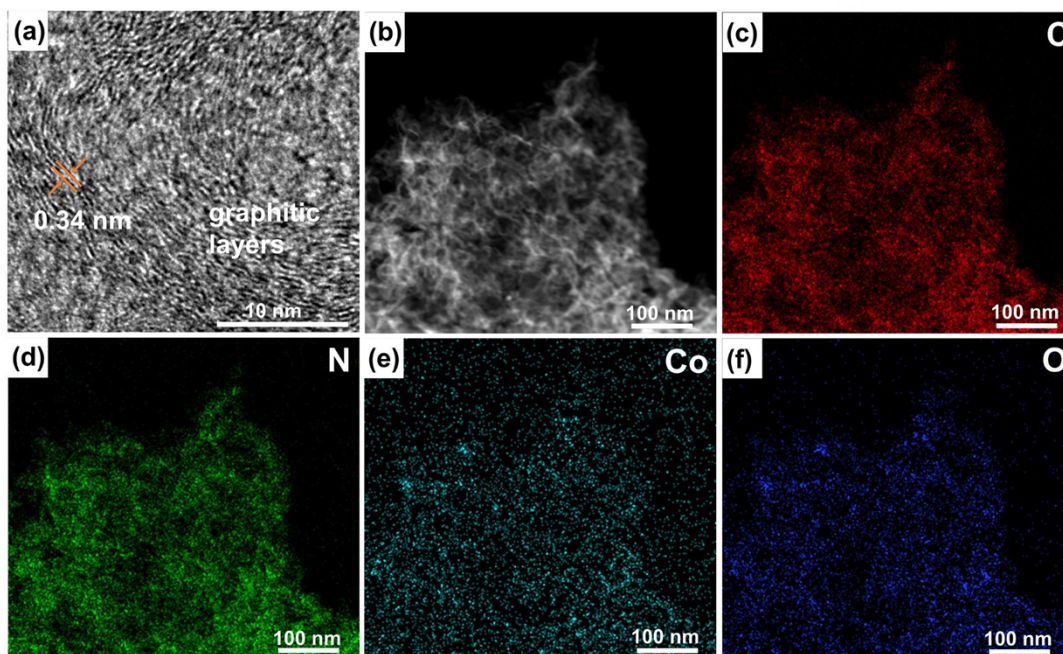


Figure S6 (a) HRTEM images and graphitic layers of Co/NC. (b) HRTEM images and the corresponding element maps showing the elements distribution of C (red), N (green), Co (blue) and O (dark blue), respectively.

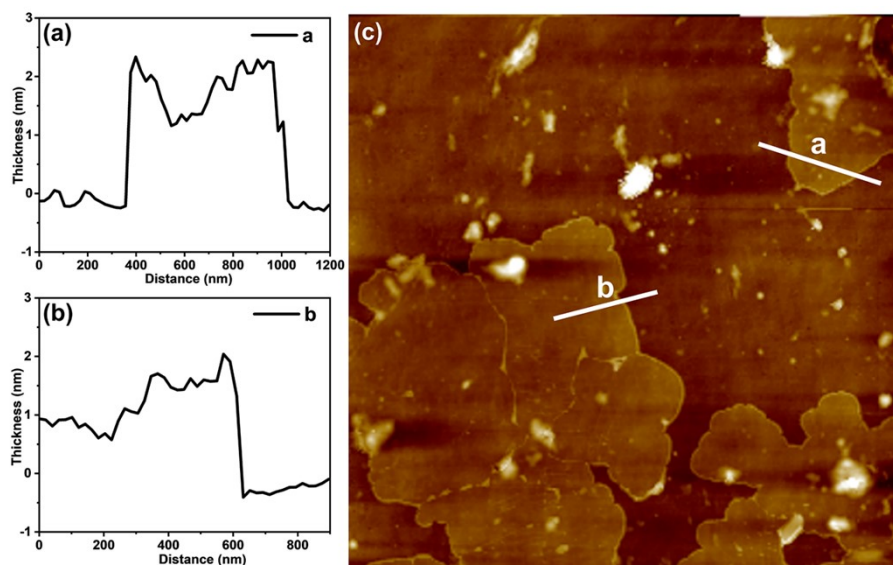


Figure S7 AFM images of Co/NC and the corresponding thickness of Co/NC.

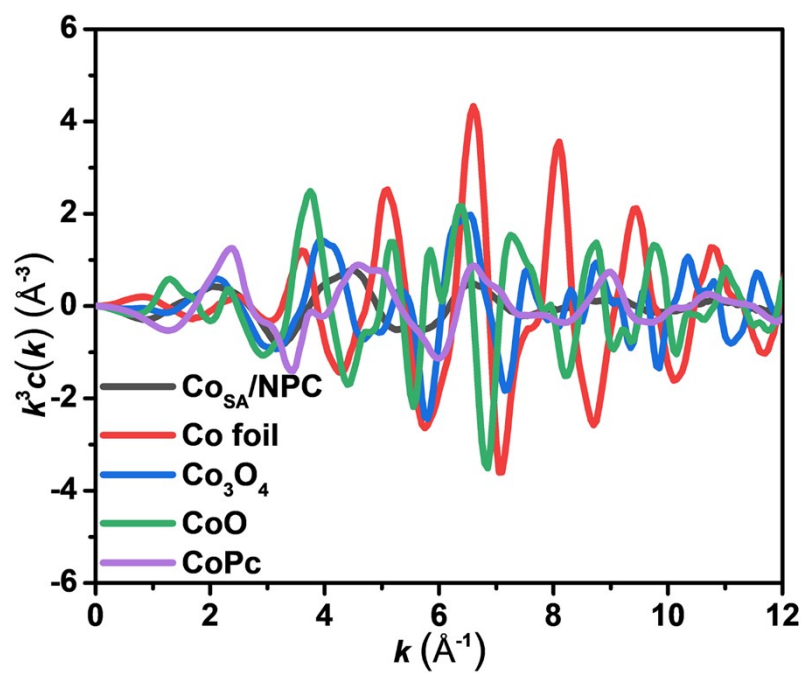


Figure S8 k^3 -weighted EXAFS in K -space for $\text{Co}_{\text{SA}}/\text{NPC}$, Co foil, Co_3O_4 , CoO and CoPC.

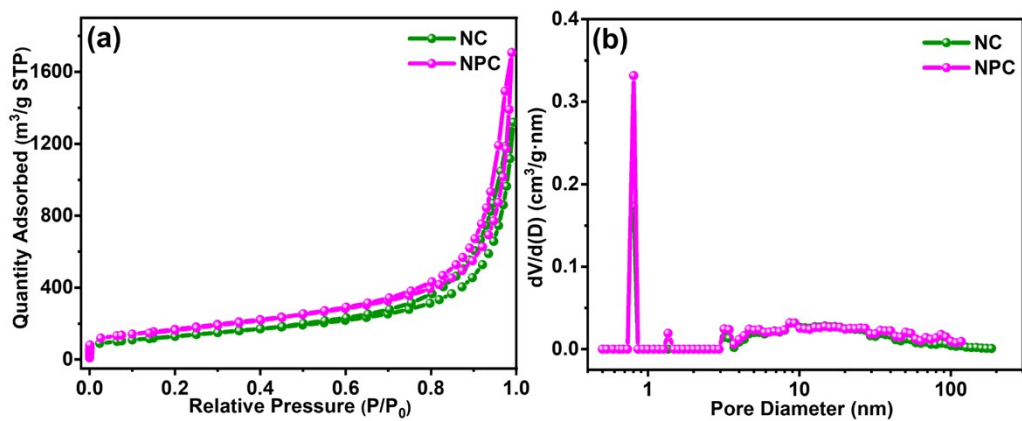


Figure S9 (a) Nitrogen adsorption–desorption isotherm spectra and (b) pore size distribution (PSD) curves of NC and NPC.

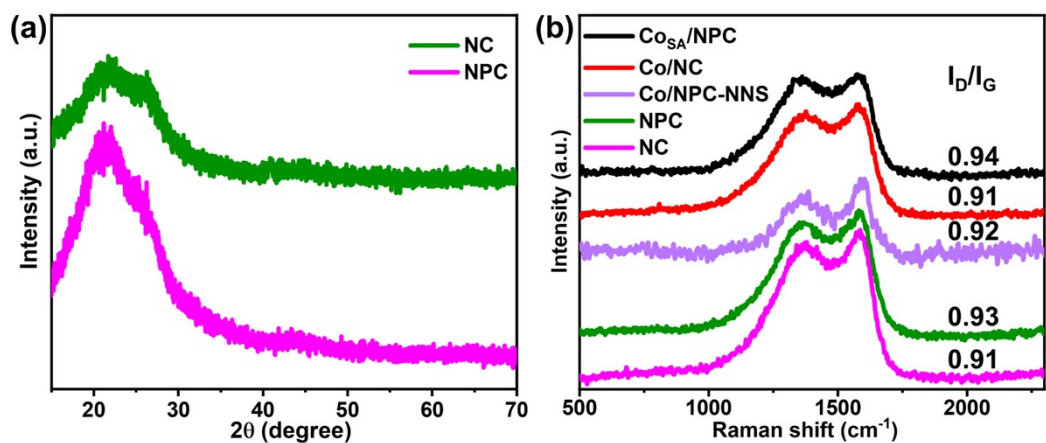


Figure S10 (a) XRD spectra of NC and NPC. (b) Raman spectra and I_D/I_G data of Co_{SA}/NPC, Co/NC, Co/NPC-NNS, NPC and NC.

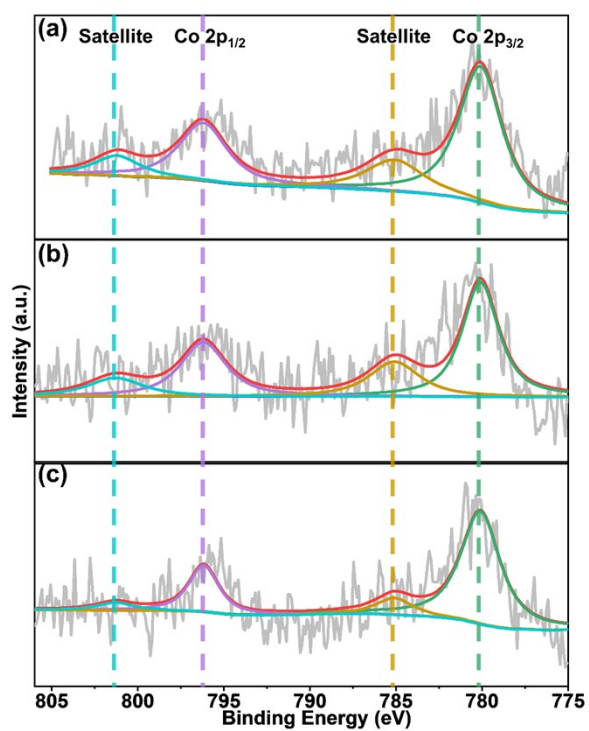


Figure S11 High resolution XPS Co 2p spectra of Co_{SA}/NPC, Co/NC and Co/NPC-NNS.

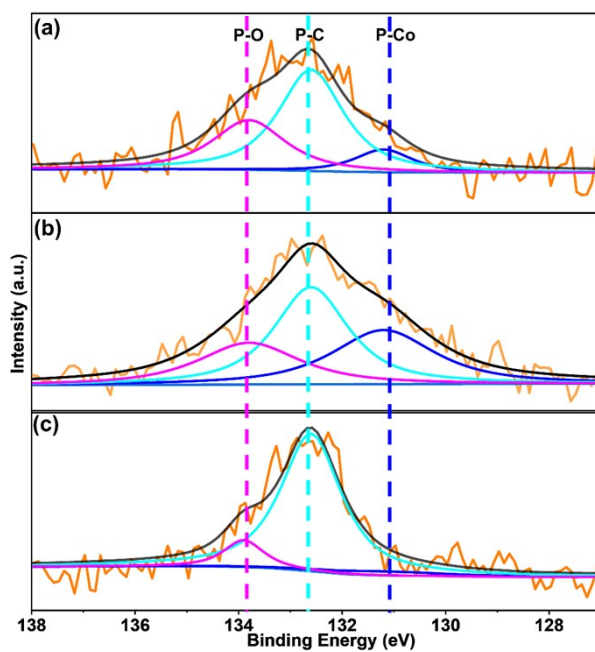


Figure S12 High resolution XPS P 2p spectra of (a) Co_{SA}/NPC, (b) Co/NPC-NNS and (c) NPC.

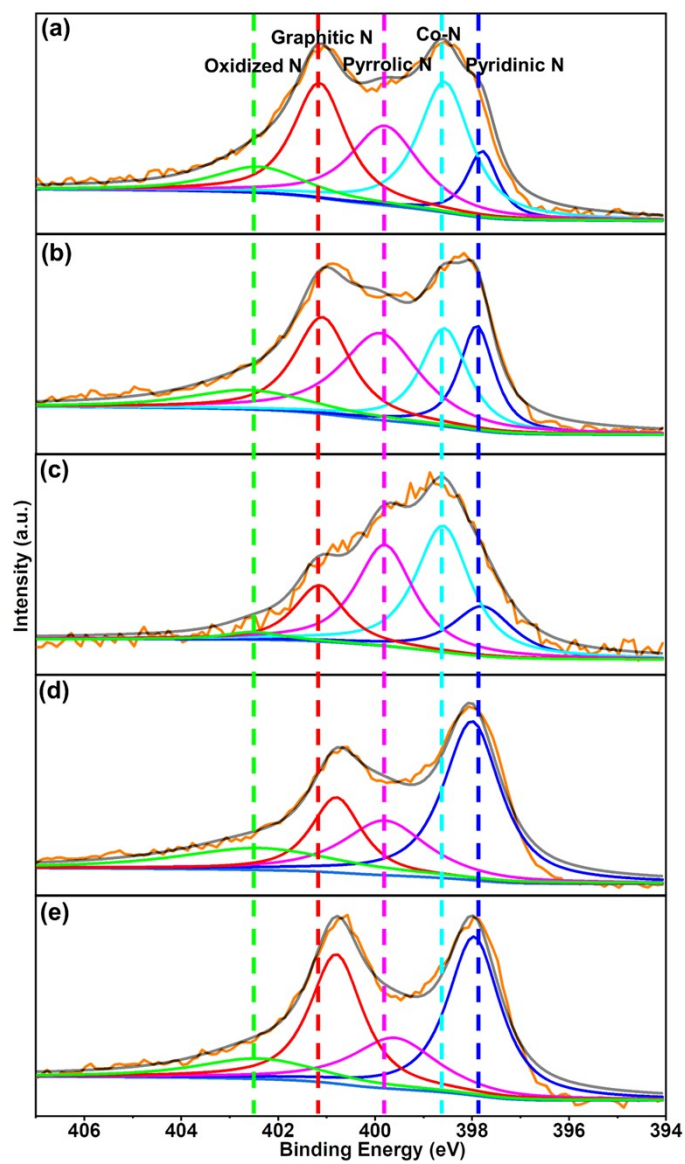


Figure S13 High resolution XPS N1s spectra of (a) Co_{SA}/NPC, (b) Co/NC, (c) Co/NPC-NNS, (d) NPC and (e) NC.

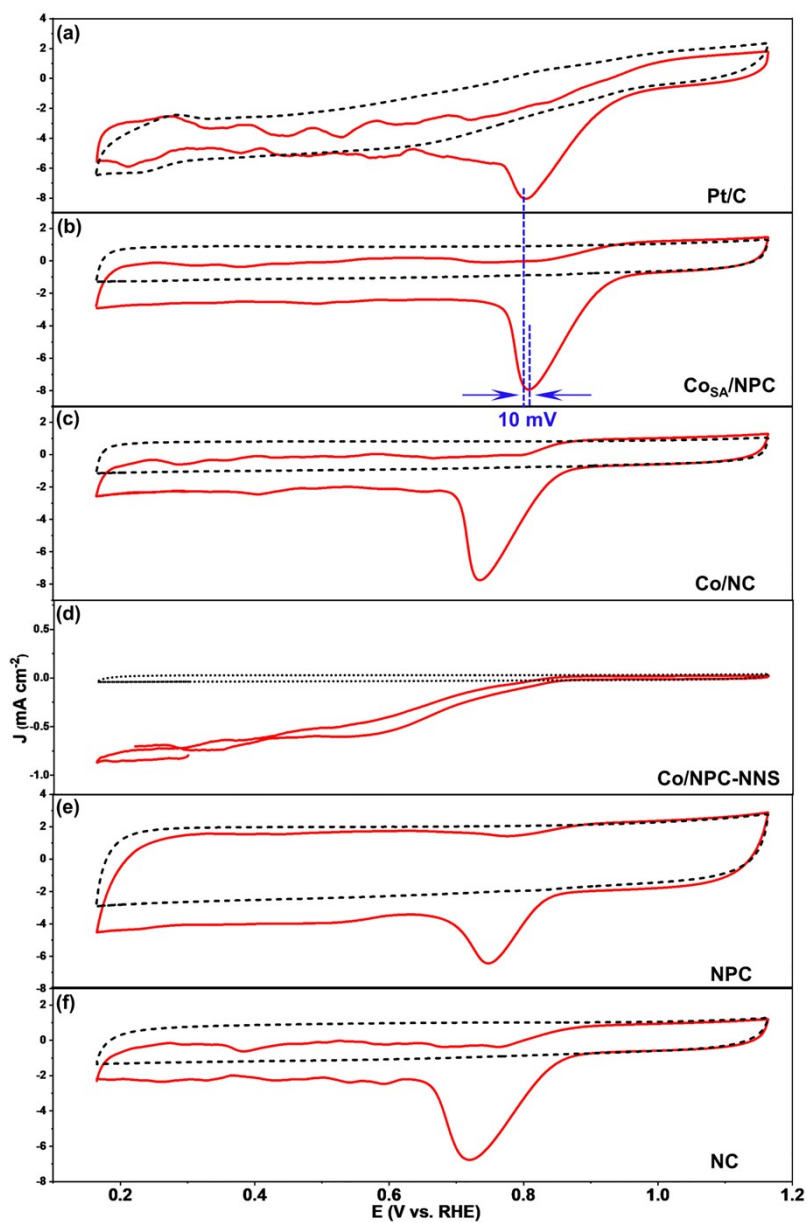


Figure S14 CV curves of different catalysts in N_2 - (black dotted line) and O_2 - (red line) saturated 0.1 M KOH solution at a scan rate of 50 mVs^{-1} : (a) Pt/C, (b) $\text{Co}_{\text{SA}}/\text{NPC}$, (c) Co/NC, (d) Co/NPC-NNS, (e) NPC and (f) NC.

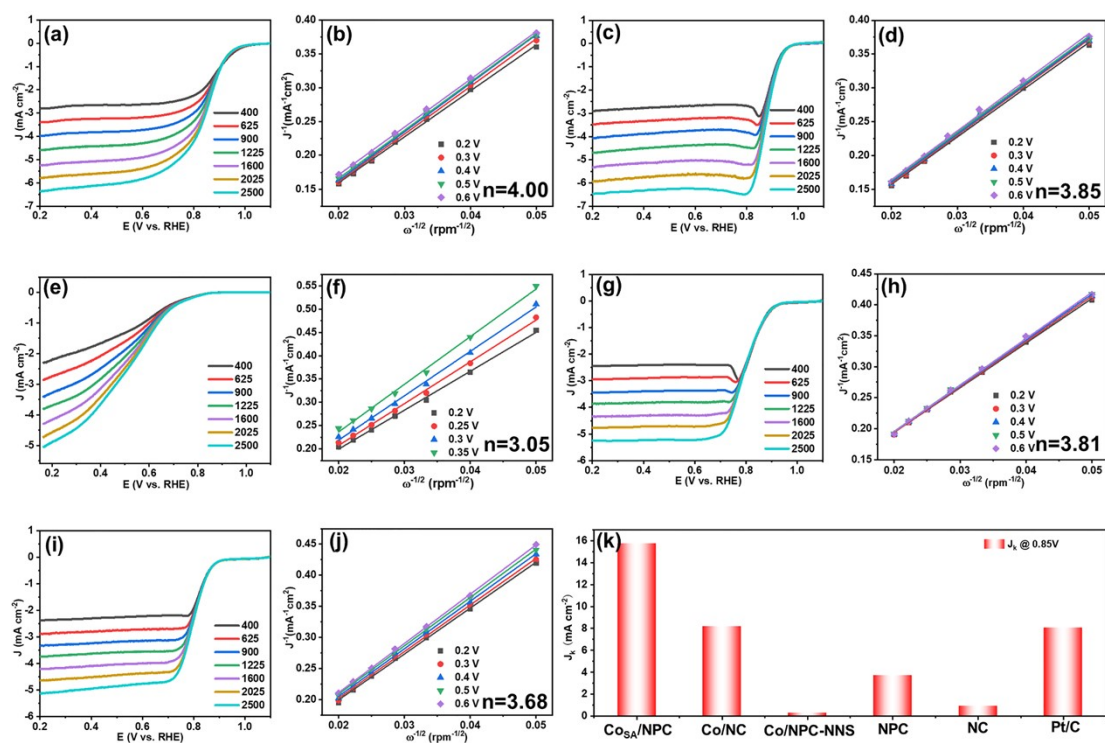


Figure S15 LSV curves of (a) Pt/C, (c) Co/NC, (e) Co/NPC-NNS, (g) NPC and (i) NC at different rotating speeds from 400 to 2500 rpm in 0.1 M KOH, respectively. The corresponding K-L plots at different potentials, (b) Pt/C, (d) Co/NC, (f) Co/NPC-NNS, (h) NPC and (j) NC, respectively. (k) Comparison of the kinetic current density (J_k) at 0.85 V (vs. RHE) for various catalysts.

As revealed in Figure S15k, the $\text{Co}_{\text{SA}}/\text{NPC}$ catalyst shows the highest diffusion kinetic current density (J_k) of 15.72 mA cm^{-2} , which is much higher than others (8.15 mA cm^{-2} for Co/NC, 0.25 mA cm^{-2} for Co/NPC-NNS, 3.68 mA cm^{-2} for NPC, 0.89 mA cm^{-2} for NC, 8.04 mA cm^{-2} for Pt/C). These results indicate the excellent ORR performance of $\text{Co}_{\text{SA}}/\text{NPC}$ catalyst.

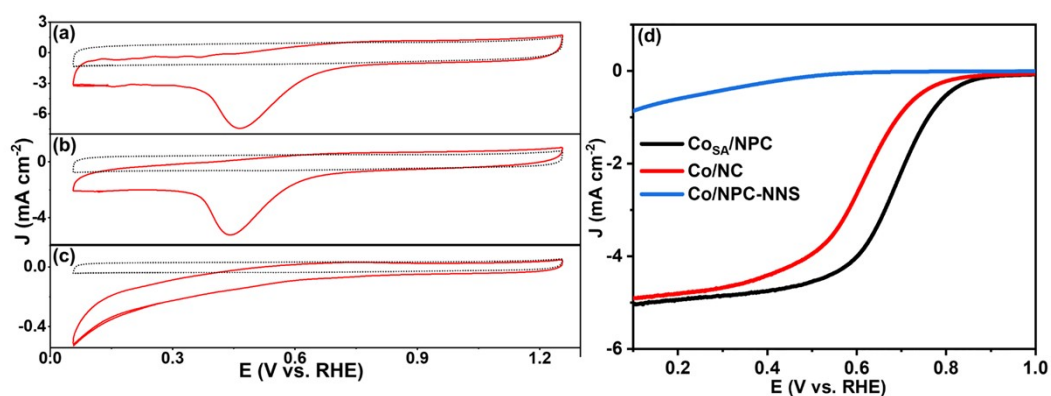


Figure S16 CV curves of different catalysts in N_2 - (black dotted line) and O_2 - (red line) saturated 0.1 M HClO_4 solution at a scan rate of 50 mVs^{-1} , (a) $\text{Co}_{\text{SA}}/\text{NPC}$, (b) Co/NC , (c) $\text{Co}/\text{NPC-NNS}$. (d) LSV curves in O_2 -saturated 0.1 M HClO_4 with a rotation rate of 1600 rpm.

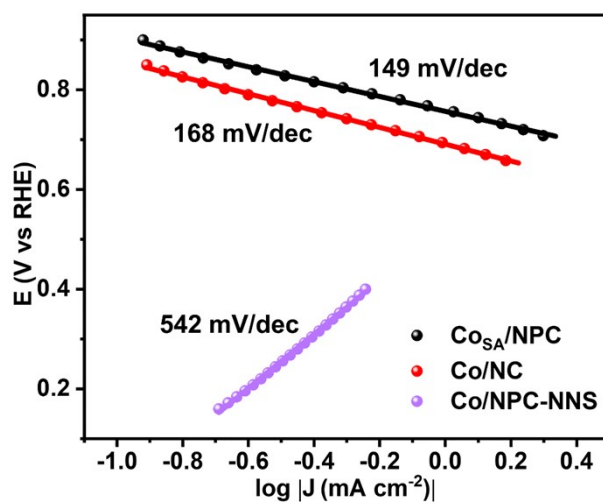


Figure S17 Tafel plots and slopes of $\text{Co}_{\text{SA}}/\text{NPC}$, Co/NC and $\text{Co}/\text{NPC-NNS}$ during ORR in 0.1 M HClO_4 .

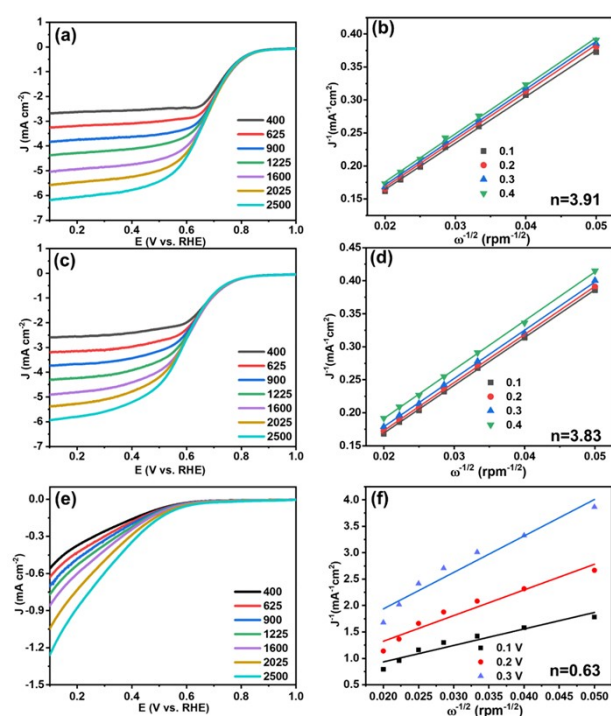


Figure S18 LSV curves of (a) Co_{SA}/NPC, (c) Co/NC, (e) Co/NPC-NNS at different rotating speeds from 400 to 2500 rpm in 0.1 M HClO₄, respectively. The corresponding K-L plots at different potentials, (b) Co_{SA}/NPC, (d) Co/NC, (f) Co/NPC-NNS.

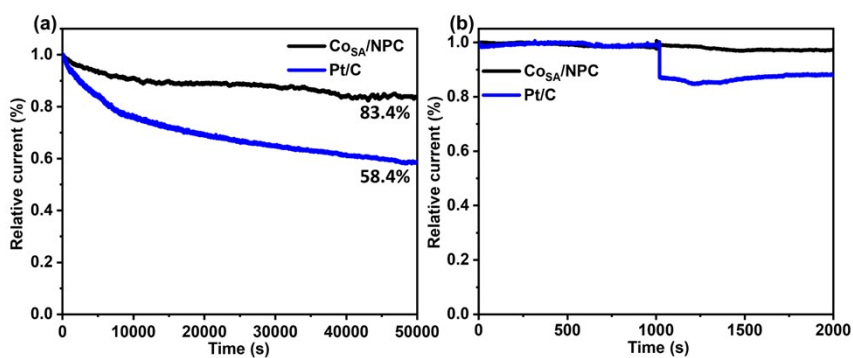


Figure S19 (a) $i-t$ chronoamperometric responses of Co_{SA}/NPC and Pt/C catalysts. (b) Chronoamperometric responses of Co_{SA}/NPC and Pt/C catalysts before and after adding of 0.5 M methanol.

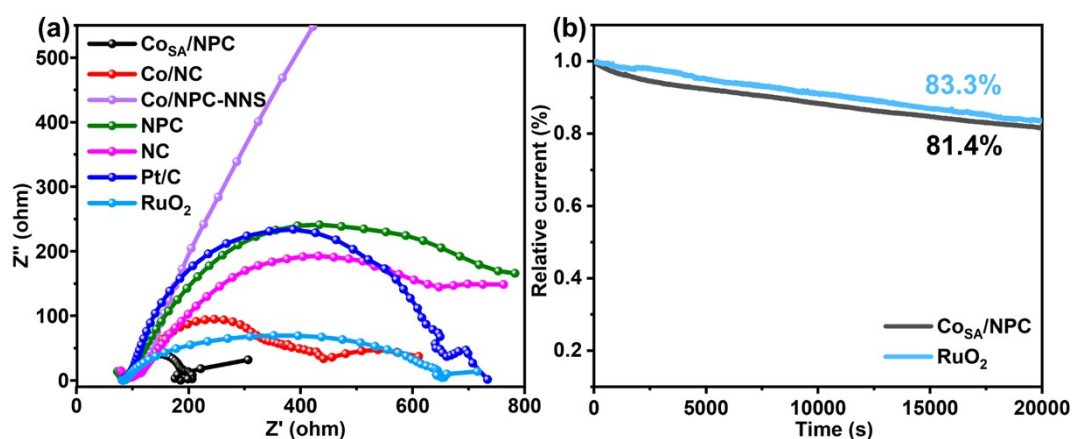


Figure S20 (a) Electrochemical impedance spectroscopy plots of $\text{Co}_{\text{SA}}/\text{NPC}$, Co/NC , $\text{Co}/\text{NPC-NNS}$, NPC , NC , Pt/C and RuO_2 at 1.68 V. (b) $i-t$ chronoamperometric responses of $\text{Co}_{\text{SA}}/\text{NPC}$ and RuO_2 catalysts for 20000s.

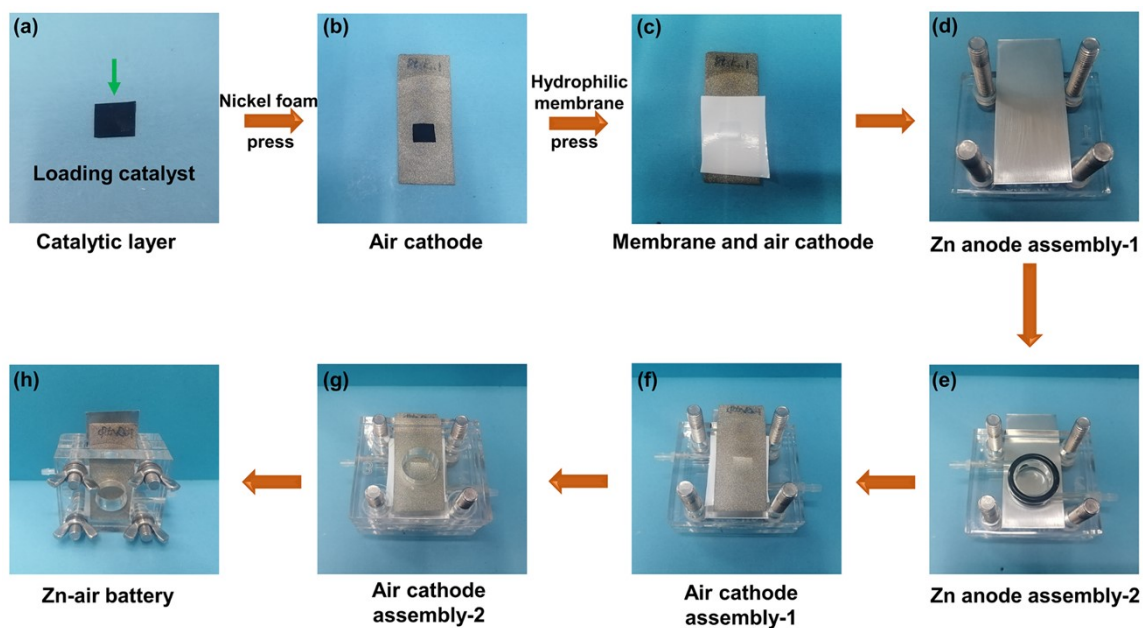


Figure S21 Photographs of the assembly process of Zn-air battery: (a) catalytic layer, (b) air cathode, (c) hydrophilic membrane and air cathode, (d) Zn anode assembly-1, (e) Zn anode assembly-2, (f) air cathode assembly-1, (g) air cathode assembly-2, (h) Zn-air battery.

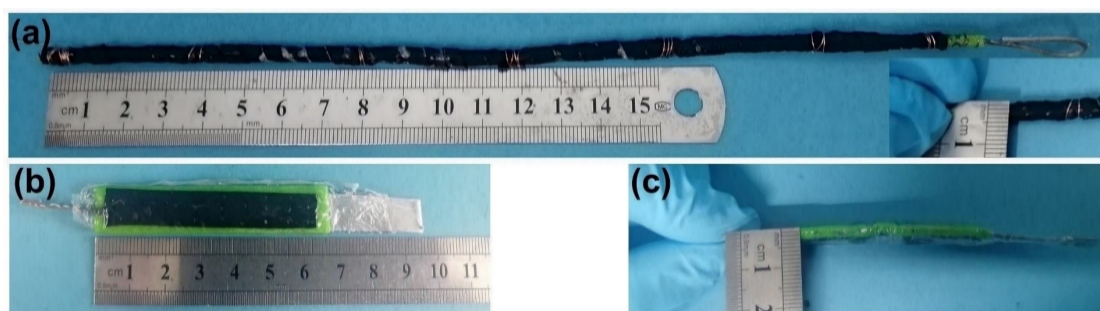


Figure S22 (a) Photos of the homemade 1D ZAB, (b) and (c) Photos of the homemade 2D ZAB.

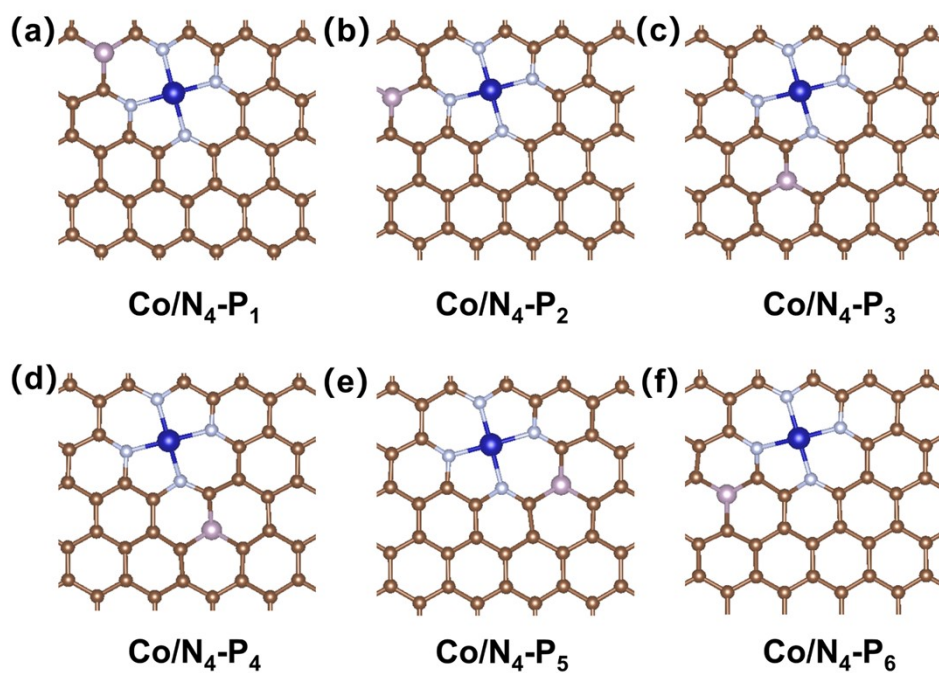


Figure S23 Computational models of Co-N₄ active sites with different positions of P dopant: (a) Co/N₄-P₁, (b) Co/N₄-P₂, (c) Co/N₄-P₃, (d) Co/N₄-P₄, (e) Co/N₄-P₅ and (f) Co/N₄-P₆.

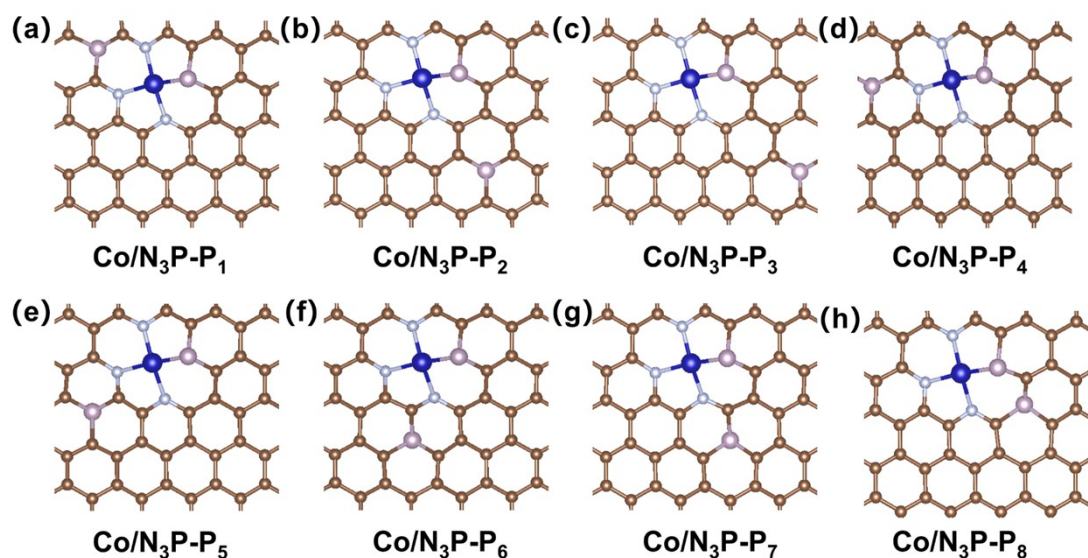


Figure S24 Computational models of Co/N₃P active sites with different positions of P dopant: (a) Co/N₃P-P₁, (b) Co/N₃P-P₂, (c) Co/N₃P-P₃, (d) Co/N₃P-P₄, (e) Co/N₃P-P₅, (f) Co/N₃P-P₆, (g) Co/N₃P-P₇ and (h) Co/N₃P-P₈.

Table S1. EXAFS fitting parameters at the Co K-edge for various samples ($S_0^2=0.778$).

Sample	Shell	N	$R(\text{\AA})$	$\sigma^2(\text{\AA}^2)$	$\Delta E_0(\text{eV})$	R factor
Co foil	Co-Co	12*	2.49(0.01)	0.0061(0.0003)	6.3(0.4)	0.0009
Co _{SA} /NPC	Co-N	2.9(0.6)	1.87(0.02)	0.0053(0.0026)	-6.2(3.0)	0.0091
	Co-P	0.9(0.3)	2.23(0.05)			

N , coordination number; R , distance between absorber and backscatter atoms; σ^2 , Debye-Waller factor to account for both thermal and structural disorders; ΔE_0 , inner potential correction; R factor indicates the goodness of the fit. S_0^2 was fixed to 0.778, according to the experimental EXAFS fit of Co foil by fixing CN as the known crystallographic value. Fitting range: $3.0 \leq k \leq 12.5$ and $1.5 \leq R \leq 2.8$ (Co foil); $3.0 \leq k \leq 11.2$ and $1.0 \leq R \leq 2.5$ (Co_{SA}/NPC).

Table S2 Summary of the N₂ sorption data for different catalysts.

Samples	SBET (m ² /g)	S _{micro} (m ² /g)	S _{meso+macro} (m ² /g)	V _{total} (cm ³ /g)	Average Pore Size (nm)
Co _{SA} /NPC	563.95	9.36	554.59	2.41	17.09
Co/NC	457.03	5.65	451.38	1.85	16.23
Co/NPC-NNS	46.55	0.02	46.53	0.06	4.18
NPC	603.75	8.06	595.69	2.64	17.50
NC	465.16	16.87	448.29	2.04	17.56

Table S3 Elemental contents of C, N, O, P and Co based on XPS analysis for the catalysts.

	Chemical composition (at%)					Co (wt%)
	C	N	O	P	Co	
Co _{SA} /NPC	83.45	7.83	7.51	0.96	0.25	1.14
Co/NC	84.61	8.02	7.14	-	0.23	1.08
Co/NPC-NNS	88.94	3.52	6.84	0.7	0.24	1.12
NPC	85.3	9.07	4.71	0.82	-	-
NC	87.15	6.75	6.10	-	-	-

Table S4 Co contents of Co_{SA}/NPC, Co/NC, Co/NPC-NNS catalysts measured by ICP, wt%.

Catalysts	Co content (measured by ICP, wt%)
Co _{SA} /NPC	1.07
Co/NC	0.92
Co/NPC-NNS	1.16

Table S5 Comparison of ORR/OER properties for Co_{SA}/NPC with reported nonprecious metal-based bifunctional electrocatalysts.

Catalysts	ORR E _{1/2} (V)	OER E _{j=10} (V)	ΔE(V)	References
Co_{SA}/NPC	0.87	1.67	0.80	This work
Co ₁ -NC/Ni ₁ -CN	0.84	1.64	0.80	Nano Res., 2021, 10.1007/s12274-021- 3535-4
Ni-N ₄ /GHSs/Fe-N	0.83	1.62	0.79	Adv. Mater., 2020, 2003134
CoNi-SAs/NC	0.76	1.57	0.81	Adv. Mater., 2019, 31, 1905622
Fe-N/P-C-700	0.867	1.66	0.793	J. Am. Chem. Soc., 2020, 142, 2404-2412
Co-N _x -By-C	0.83	1.66	0.83	ACS Nano, 2018, 12, 2, 1894–1901
Fe/NSDC	0.84	1.64	0.80	Small, 2019, 15, 1900307
NC@Co-NGC DSNCs	0.82	1.64	0.82	Adv. Mater. 2017, 29, 1700874
Co-POC	0.83	1.70	0.87	Adv. Mater., 2019, 31, 1900592
NC@Co-NGC DSNCs	0.82	1.64	0.82	Adv. Mater., 2017, 29, 1700874
Co@Co ₃ O ₄ /NC-1	0.80	1.65	0.85	Angew. Chem. Int. Ed., 2016, 55, 4087-4091
MnCo ₂ O ₄ /NCNT	0.82	1.68	0.86	J. Am. Chem. Soc., 2014, 136, 7551-7554
NiCo@N-C	0.76	1.78	1.02	Adv. Funct. Mater., 2017, 28, 1705094
NiO/CoN PINWs	0.68	1.55	0.87	ACS Nano, 2017, 11, 2275
NiCo ₂ S ₄ @N/S- rGO	0.76	1.70	0.94	Energy Environ. Sci. 2018, 11, 3375.
CaMnO ₃	0.76	1.77	1.01	Adv. Mater. 2014, 26, 2047

Table S6 The performance of aqueous rechargeable Zn-air batteries with reported transition metal-based electrocatalysts.

Catalysts	OCP (V)	Power density (mW cm ⁻²)	Specific capacity (mAh gZn ⁻¹)	charge/discharge voltage gap (V)	References
Co_{SA}/NPC	1.49	204.3	752.6@10	0.84@5	This work
CoNiSAs/NC	1.45	101.4	750.9@20	0.82@5	Adv. Mater., 2019, 1905622
Ni-N ₄ /GHSs/Fe-N ₄	1.45	-	777.6@5	0.88@10	Adv. Mater., 2020, 2003134
CoN ₄ /NG	1.51	115	730@100	0.84@10	Nano Energy, 2018, 50, 691
Co-N,B-CSs	1.43	100.4	-	1.35@5	ACS Nano, 2018, 12, 1894
CoNCF-1000-80	1.44	170	650@10	0.73@10	Small, 2018, 14, 1703739
CoZn-NC-700	1.42	152	578@10	0.73@10	Adv. Funct. Mater., 2017, 27, 1700795
PtPd Film/Ni Foam	1.52	111	613@10	-	ACS Sustainable Chem. Eng., 2018, 6, 9, 12367
NiCo ₂ O ₄	1.45	-	580@20	~0.7@20	Nanoscale, 2014, 6, 3173
CoNi/NG	-	~130.5	-	0.77@10	Carbon, 2019, 144, 8-14
nNiFe LDH/3D MPC	1.51	98	530@10	0.82@10	J. Mater. Chem. A, 2018,6, 14299
NCNT/Co O-NiONiCo	-	-	594@7	0.86@50	Angew. Chem., Int. Ed., 2015, 54, 9654
Co ₃ O ₄ -doped Co/CoFe	1.43	97	727@20	~0.7@5	J. Mater. Chem. A, 2018, 6, 3730

The number behind @ is current density (mA/cm²) during test.

Table S7 The performances of solid-state rechargeable Zn-air batteries with reported electrocatalysts using KOH and poly(vinyl alcohol) (PVA) as gel electrolyte.

Catalysts	OCP (V)	Charge/discharge voltage gap (V)	Flexibility	References
Co_{SA}/NPC (1D ZABs)	~ 1.36	~ 0.82@1	Benting into one rings, two ring and three rings	This work
Co_{SA}/NPC (2D ZABs)	~ 1.28	~ 0.73@1	Benting into 30°-150°	
NGM-Co	1.439	0.70@1	Benting into 90° and 180°	Adv. Mater., 2017, 29, 1703185
CoNi-SAs/NC	-	~0.78@1	Benting into 30°-150°	Adv. Mater., 2019, 31, 1905622
Co-N,B-CSs	1.345	-	-	ACS Nano, 2018, 12, 1894
N-GDY-900 (1D ZABs)	1.25	~0.75@2	Benting into one and two rings	Nano Energy, 2021, 85, 106024
N-GDY-900 (2D ZABs)	1.23	~0.79@2	Benting into 60°, 90° and 120°	

The number behind @ is current density (mA/cm²) during test.

Table S8. Adsorption free energy of different intermediates in ORR for Co/N₄, Co/N₄-P₁ to P₆, Co/N₃P, and Co/N₃P-P₁ to P₈.

ΔG_{ads} (eV)	OOH*	O*	OH*
Co/N ₄	4.156	2.643	1.075
Co/N ₃ P	4.137	2.335	1.063
Co/N ₄ -P1	4.305	2.530	1.195
Co/N ₄ -P2	4.234	2.516	1.039
Co/N ₄ -P3	4.198	2.363	1.078
Co/N ₄ -P4	4.084	2.518	1.024
Co/N ₄ -P5	3.915	2.242	0.787
Co/N ₄ -P6	4.200	2.364	1.075
Co/N ₃ P-P1	4.250	2.410	1.134
Co/N ₃ P-P2	3.999	2.177	0.946
Co/N ₃ P-P3	4.016	2.715	0.939
Co/N ₃ P-P4	3.942	2.137	0.882
Co/N ₃ P-P5	3.871	2.036	0.812
Co/N ₃ P-P6	4.042	2.233	0.972
Co/N ₃ P-P7	4.127	2.389	1.108
Co/N ₃ P-P8	3.966	2.388	2.388

References

- [1] Kresse, G., *Phys. Rev. B* **1996**, 54, 11169-11186.
- [2] G. Kresse, D. Joubert, *Phys. Rev. B* **1999**, 59, 1758-1775.
- [3] J.P. Perdew, K. Burke, M. Ernzerhof, *Energy Environ. Sci.* **1996**, 77, 3865-3868.
- [4] S. Grimme, J. Antony, S. Ehrlich, H. Krieg, *Chem. Phys.* **2010**, 132, 154104-154100.
- [5] A.A. Peterson, F. Abild-Pedersen, F. Studt, J. Rossmeisl, J.K. Nørskov, *Energy Environ. Sci.* **2010**, 3 1311-1315.